PHYSICAL REVIEW E **98**, 033201 (2018)

Thin target charging in short laser pulse interactions

A. Poyé,[1,2] S. Hulin,[2] J. Ribolzi,[3] M. Bailly-Grandvaux,[2] F. Lubrano-Lavaderci,[3] M. Bardon,[3]
D. Raffestin,[2] J. J. Santos,[2] and V. Tikhonchuk[2]
[1]*Laboratoire de Physique, ENS de Lyon, Université de Lyon, CNRS, Lyon 69007, France*
[2]*Centre Lasers Intenses et Applications, University Bordeaux, CNRS, CEA, Talence 33405, France*
[3]*CEA/DAM/CESTA, BP 12, Le Barp 33405, France*

(Received 24 April 2018; published 4 September 2018)

A model of target charging in interaction with an intense short laser pulse is revised. It provides estimates of the current of energetic electrons escaping the target and the total accumulated electric charge as a function of the laser pulse characteristics and target thickness. Comparisons with experimental data show the model performance, in particular, in the case of targets thinner than the mean-free path of energetic electrons.

DOI: 10.1103/PhysRevE.98.033201

I. INTRODUCTION

Interaction of intense electromagnetic pulses with solid targets results in emission of energetic electrons and target polarization. The recharge current induces strong electromagnetic pulses (EMPs) reported in numerous publications [1–5]. With the development of high-intensity laser sources the control of the electromagnetic environment becomes an urgent and acute problem. The EMPs produced in laser target interactions may perturb normal operation of electronic devices [6] or can be used for controlled magnetic field generation [7–10]. A detailed study of the mechanisms of target charging and EMP generation has been reported in Refs. [11,12]. It was demonstrated that target polarization is due to the energetic electrons ejected from the laser focal zone, and an EMP in the GHz frequency range is induced by the neutralization current flowing to the ground through the target holder. For the picosecond laser pulses, the polarization and neutralization stages are separated in time and can be considered separately. In particular, the problem of target charging, in the case where the electron mean-free path is smaller than the target thickness, was considered in Ref. [13]. The case of thin targets needs special attention as the recirculation of energetic electrons may increase the electron emission current and consequently the EMP strength. This could be penalizing for such short laser pulse applications as the x-ray and proton radiography [14–16] of living cells or small organisms.

The present paper presents an extension of the model developed in Refs. [11–13] to the case of thin targets. The major element is an approximate model for the hot electron distribution function in the target, which is indispensable for evaluation of electron emission from the rear target side. The electrons may escape from the both, front, and rear sides of the target, but their current is controlled by the common potential barrier depending on the target thickness. In particular, for the target thickness smaller than the hot electron Debye length, the electron density is strongly modified as well as the potential barrier. The revised model provides a description of the hot electron distribution function and applies to both thin and thick targets. Its validity is demonstrated by a comparison with the experimental data obtained in interaction of subpicosecond laser pulses with thin targets.

The paper is organized as follows: Sec. II outlines the main elements of the target charging model and presents elements related to the electron distribution function. Section III provides a comparison of the model with the experiments. The details related to the potential calculation and numerical realization are presented in the appendices. The main results are summarized in Sec. IV.

II. MODEL OF THE TARGET POLARIZATION

The problem of target polarization and subsequent EMP emission in laser target interaction requires intensive numerical simulations with electromagnetic, kinetic, and hydrodynamic codes [11], which are time consuming. This is the motivation for developing a simplifying model retaining the major physics elements and providing a quick evaluation of the polarization charge and the EMP amplitude, with a precision sufficient for designing the diagnostic equipment and protection of electronic devices in the interaction chamber.

Our model describes a self-consistent evolution of the hot electron density and the target electrostatic potential energetic electrons escaping the target and the total accumulated electric charge as a function of the laser pulse and target parameters. The core of the model is the hot electron distribution function $f(\varepsilon, t)$ inside the target. Its integral represents the total number of hot electrons, $N(t) = \int f(\varepsilon, t)\, d\varepsilon$, and evolves in time according to Eq. (1), where the right-hand side describes the hot electron creation by the laser (first term), the cooling due to collisions with the target electrons (second term), and the electron ejection (third and fourth terms):

$$\partial_t f(\varepsilon, t) = \frac{1}{t_{\mathrm{las}}} f_{\mathrm{las}}(\varepsilon)\, \Theta(t_{\mathrm{las}} - t) - \frac{1}{t_{ee}(\varepsilon)} f(\varepsilon, t) - g_{\mathrm{fr}}(\varepsilon, t) - g_{\mathrm{re}}(\varepsilon, t). \quad (1)$$

Here Θ is the Heaviside function, t_{las} is the laser pulse duration, t_{ee} is the cooling time depending on the electron energy ε, and

g_{fr} and g_{re} are the rates of electron ejection from the front and the rear side of the target, respectively. These terms are detailed in the following sections.

This model presents a different paradigm in the hot electron cloud description. The previous model was a concatenation of a steady state during the laser pulse and a global cooling after the laser pulse. In the first step, the electron energy was maintained by the laser and the number of electrons was defined by an equilibrium between the electron production and the cooling. The second step corresponded to the global cooling of all remaining electrons while keeping their number constant. In this model, the energy of each hot electron is assumed to be constant during their cooling time. The global cooling is accounted by the reduction of their number in Eq. (1).This constant energy approximation may globally overestimate the mean electron energy over their lifetime by a factor of two. However, because of this approximation, we are able to provide a detailed description of the distribution function and detailed evolution of the ejection current.

A. Laser heating

The action of the laser pulse is described in a simplified manner as the source of hot electrons of a constant power operating for a time period t_{las}. The energy distribution of hot electrons inside the target is supposed to be exponential:

$$f_{\mathrm{las}}(\varepsilon) = (N_0/T_0)\,\exp(-\varepsilon/T_0). \tag{2}$$

The total energy of hot electrons in the target, $N_0 T_0 = \eta \mathcal{E}_{\mathrm{las}}$, is a fraction η of the laser pulse energy $\mathcal{E}_{\mathrm{las}}$. The initial hot electron temperature T_0 is defined by the laser pulse intensity and wavelength according to Refs. [17,18] for subrelativistic intensities or the ponderomotive scaling [19] for higher laser intensities:

$$T_0 = 3 m_e c^2 a_{\mathrm{las}}^{4/3}, \quad \text{for } a_{\mathrm{las}} < 0.3, \tag{3a}$$

$$T_0 = 0.47 m_e c^2 a_{\mathrm{las}}^{2/3}, \quad \text{for } a_{\mathrm{las}} \lesssim 1.1, \tag{3b}$$

$$T_0 = m_e c^2 \left(\sqrt{1 + a_{\mathrm{las}}^2} - 1\right) \text{ for } a_{\mathrm{las}} > 1.1, \tag{3c}$$

where m_e is the electron mass and c is the light velocity. These expressions agree with the experimental data within a factor of two [20]. Here the dimensionless laser vector potential is $a_{\mathrm{las}} = 0.85 \lambda_{\mathrm{las}} I_{\mathrm{las}}^{1/2}$, the laser intensity is $I_{\mathrm{las}} = 0.65 \mathcal{E}_{\mathrm{las}}/(t_{\mathrm{las}} \pi r_{\mathrm{las}}^2)$ in units of 10^{18} W cm^{-2}, and r_{las} the focal radius: half width at half maximum.

B. Electron collisional cooling

The hot electrons are cooling down in collisions with target atomic electrons and due to the bremsstrahlung emission; see Fig. 1. We define the cooling time of hot electrons t_{ee} in our simplified kinetic model as a function of the penetration rangein the target $r_m(\varepsilon)$ and the electron velocity $v(\varepsilon)$. Convenient interpolations for the nonrelativistic electrons are provided in Ref. [21] in the continuous slowing-down approximation. There the electron penetration range r_m is expressed energetic electrons escaping the target and the total accumulated electric charge as a function of its energy ε and the material parameters: the atomic number A_{tar}, the atomic charge Z_{tar}, and the target density ρ_{tar}. We extended this scaling to higher electron energies by using the tables ESTAR [22]. The extended interpolation for the electron range reads

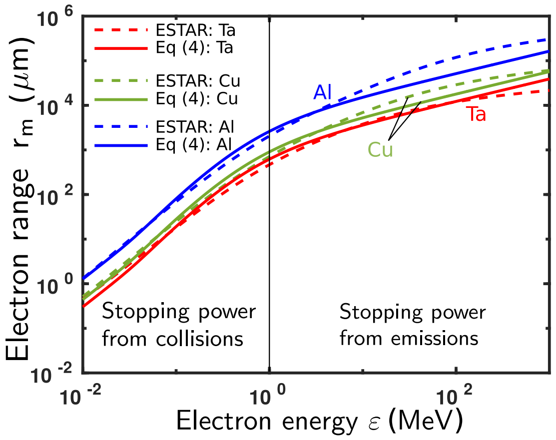

FIG. 1. Electron penetration range versus the initial electron energy for tantalum (red curves), copper (green curve), and aluminum (blue curves). The data from Ref. [22] (dashed lines) are compared with the interpolation given by Eq. (4).

$$r_m = \frac{2760 A_{\mathrm{tar}}}{\rho_{\mathrm{tar}}} \varepsilon^{5/3} Z_{\mathrm{tar}}^{-8/9} \frac{(1+\varepsilon+\varepsilon^4)^{1/8}}{(1+1.96\varepsilon^{5/3})}, \tag{4}$$

where the electron range is in microns, electron energy in MeV, and the target density in g/cc. This function is presented in Fig. 1 together with the tabulated data from Ref. [22] for tantalum and aluminum.

The dynamic range is defined following the scaling of the electron energy as a function of the distance ξ from the injection layer [21]:

$$\frac{\varepsilon(\xi)}{\varepsilon} = (1 - \xi/r_m)^{3/5}. \tag{5}$$

Expressing electron velocity in terms of energy, one finds the time needed for an electron to access the position ξ by integrating the relation $dt = d\xi/v$ over the coordinate. Then the cooling time t_{ee} is defined as the time needed for the electron to reach the stopping range:

$$t_{ee} = \int_0^{r_m} \frac{d\xi}{v}. \tag{6}$$

This integral can be taken numerically or approximated with a simple formula:

$$t_{ee}(\varepsilon) \simeq \frac{r_m(\varepsilon)}{v}, \tag{7}$$

where v is the initial electron velocity. Figure 2 shows the cooling time for several energy values according to numerical integration and the interpolation formula (7).

The hot electrons have a stochastic distribution inside the target presented in Fig. 3(a) adapted from Ref. [21]. The electrons propagate in the target until their first collision with an ion at the depth χ_E that scatters them in any direction. Several subsequent collisions homogenize the electron cloud in a truncated sphere: the electron cooling time is much longer than the time of electron elastic scattering on ions. Such a spherical segment of a radius $r_m - \chi_E$ and centered at depth

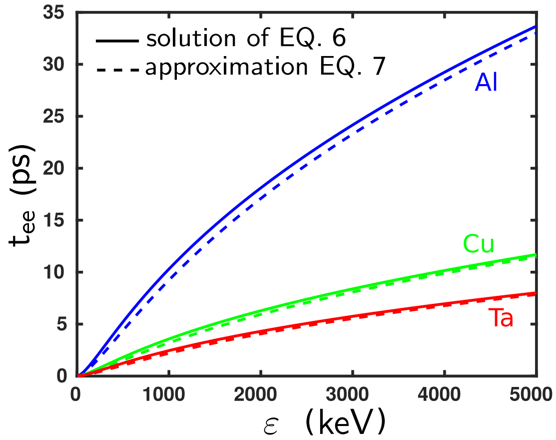

FIG. 2. Hot electron cooling time found from Eq. (6) and the approximate formula (7) for aluminum (blue), copper (green), and tantalum (red).

χ_E is approximated in our model with a cylinder of the radius $r_m(\varepsilon) - \chi_E(\varepsilon)$ and the height $r_m(\varepsilon)$. Those dimensions may be limited by the target size, respectively, the target radius $r_{\rm tar}$, and the target thickness $e_{\rm tar}$.

Integration of the equation $dt = d\xi/v$ from $\xi = 0$ to $\xi = r < r_m$ provides us with an expression for the dynamic range as a function of time. It can be approximated by

$$\xi(\varepsilon, t) \simeq \min\,[tv, r_m(\varepsilon)]. \tag{8}$$

The radial evolution is supposed to be delayed since the electrons are accelerated inwards and go in an axial direction before being scattered. To introduce this delay into the model, the radial expansion is reduced by a factor $(r_m - \chi_E)/r_m$:

$$r(\varepsilon, t) = \frac{r_m(\varepsilon) - \min\,[\chi_E(\varepsilon), e_{\rm tar}]}{r_m(\varepsilon)}\xi(\varepsilon, t). \tag{9}$$

Note that the target thickness already interferes here. For a target thinner than the collision depth χ_E, this latter is replaced by the target thickness itself since the electrons are scattered in every direction after their bounce at the target rear side; see Figs. 3(b) and 3(c).

In addition, in order to take into account the fact that hot electrons are created across the whole laser focal spot surface, we set the radius of the cylinder to be $r + r_{\rm las}$. It also may be limited by the target radius $r_{\rm tar}$. Then the electron cloud surface and volume read

$$s(\varepsilon, t) = \pi \min\,[r(\varepsilon, t) + r_{\rm las}, r_{\rm tar}]^2, \tag{10a}$$

$$\mathrm{V}(\varepsilon, t) = s(\varepsilon, t) \min\,[\xi(\varepsilon, t), e_{\rm tar}]. \tag{10b}$$

The average density of the electron cloud is estimated as a ratio of the total number of hot electrons and the average cloud volume, $n(t) = N(t)/V_{\rm av}(t)$, where

$$N(t) = \int_0^\infty f(\varepsilon, t)\, d\varepsilon, \tag{11a}$$

$$V_{\rm av}(t) = \frac{1}{N(t)} \int_0^\infty f(\varepsilon, t) \mathrm{V}(\varepsilon, t)\, d\varepsilon. \tag{11b}$$

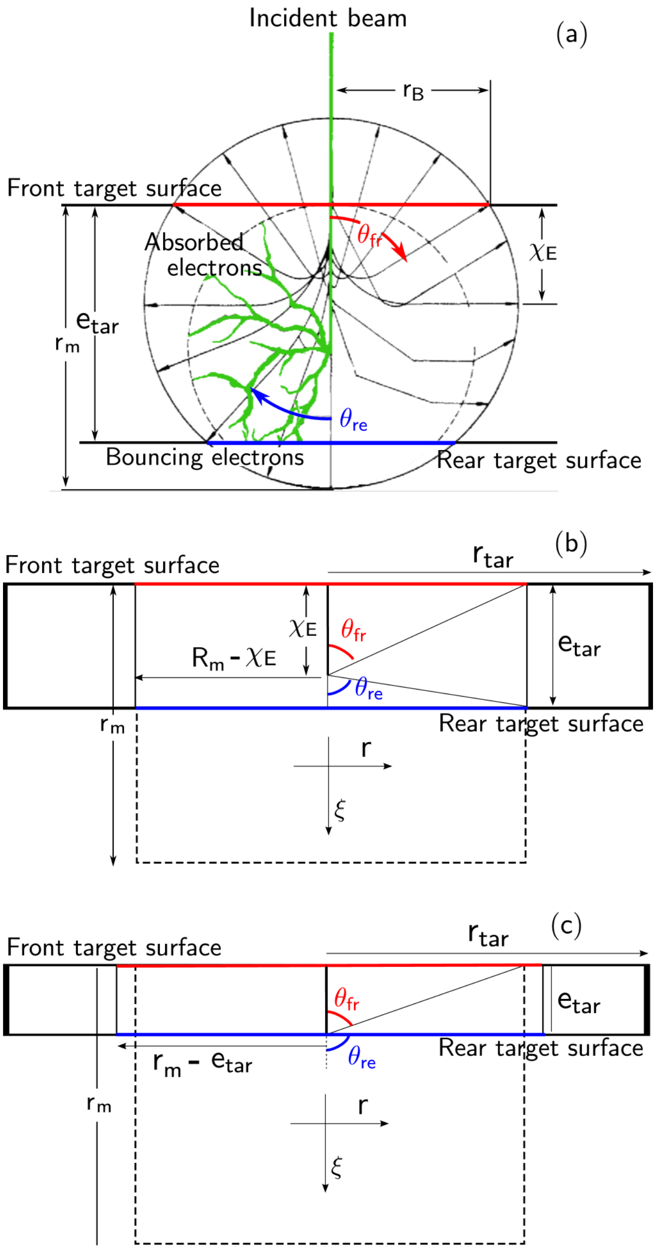

FIG. 3. (a) Scheme of a mono-energetic electron beam penetration in a target: r_m is the maximum range, the factor $\zeta = 0.187 Z_{\rm tar}^{2/3}$ accounts for the electron-ion scattering, $\chi_E = 0.5 r_m (1 + 2\zeta - 0.21\zeta^2)/(1+\zeta)^2$ is the maximum energy deposition depth, and r_B is the backscattering range. Angle $\theta_{\rm fr}$ is the maximum angle of electron ejection from the front target face, and $\theta_{\rm re}$ is the maximum ejection angle from the rear face. Figure adapted from Ref. [21] with permission. (b) Simplified geometry used for cases where $\xi(\varepsilon, t) > e_{\rm tar}$ and $\chi(\varepsilon) < e_{\rm tar}$. (c) Simplified geometry used for cases where $\xi(\varepsilon, t) > e_{\rm tar}$ and $\chi(\varepsilon) > e_{\rm tar}$.

Similarly, the average electron energy and radius are defined as

$$T(t) = \frac{1}{N(t)} \int_0^\infty \varepsilon f(\varepsilon, t)\, d\varepsilon, \tag{12a}$$

$$R_{\rm av}(t) = \frac{1}{N(t)} \int_0^\infty f(\varepsilon, t) \min\,[r(\varepsilon, t) + r_{\rm las}, r_{\rm tar}]\, d\varepsilon. \tag{12b}$$

These averaged values are used to define the average Debye length of the hot electrons:

$$\lambda_{\mathrm{Dh}}(t)=\sqrt{\epsilon_0 V_{\mathrm{av}} T/e^2 N}. \tag{13}$$

C. Electron ejection current

Knowing the hot electron distribution function inside the target, one can readily estimate the flux of escaping electrons. The scheme in Fig. 3(a) shows the electrons ejected from the front surface from the circle of an area πr_B^2 within a cone with the opening angle θ_{fr}. If the target is thin enough, a second emission surface may appear when the hot electrons reach the rear surface. In the cylindrical geometry shown in Fig. 3(b), the ejection surface is defined by the angles $\theta_f r$ and θ_{re}. In the case $e_{\mathrm{tar}} > \chi_E$, we define the ejection angle from the center of the sphere at χ_E as follows:

$$\theta_{\mathrm{fr}}(\varepsilon,t)=\arctan\frac{r(\varepsilon,t)}{\chi_E}, \tag{14a}$$

$$\theta_{\mathrm{re}}(\varepsilon,t)=0 \quad \text{if } \xi(\varepsilon,t)<e_{\mathrm{tar}}, \tag{14b}$$

$$\theta_{\mathrm{re}}(\varepsilon,t)=\arctan\frac{r(\varepsilon,t)}{e_{\mathrm{tar}}-\chi_E} \quad \text{if } \xi(\varepsilon,t)>e_{\mathrm{tar}}. \tag{14c}$$

Figure 3(c) illustrates the case where $e_{\mathrm{tar}} < \chi_E$. The center of the scattering sphere is at the target rear side where the major part of electrons are reflected back in the target. Then the ejection angles are defined as

$$\theta_{\mathrm{fr}}(\varepsilon,t)=\arctan\frac{r(\varepsilon,t)}{e_{\mathrm{tar}}}, \tag{15a}$$

$$\theta_{\mathrm{re}}(\varepsilon,t)=0 \quad \text{if } \xi(\varepsilon,t)<e_{\mathrm{tar}}, \tag{15b}$$

$$\theta_{\mathrm{re}}(\varepsilon,t)=\pi/2 \quad \text{if } \xi(\varepsilon,t)>e_{\mathrm{tar}}. \tag{15c}$$

Note regarding $r(\varepsilon,t)>r_{\mathrm{tar}}$ that the ejections can be ejected in any directions: θ_{fr} and θ_{re} are set to $\pi/2$. This may happen for a small target at a high laser intensity. We recall that our model applies to disk-shaped targets ($r_{\mathrm{tar}} > e_{\mathrm{tar}}$).

The ejection current is composed of hot electrons escaped from the front and rear target surfaces and able to overcome the potential barrier $\Phi(t)$ builtat the target surfaces. The flux of electrons ejected in the cone with the angle θ_{fr} or θ_{re} through the surface s reads

$$g_{\mathrm{fr}}(\varepsilon,t)=\frac{vf(\varepsilon,t)}{\min[\xi(\varepsilon,t),e_{\mathrm{tar}}]}\sin^2(\theta_{\mathrm{fr}}/2)\,\Theta(\varepsilon-e\Phi), \tag{16a}$$

$$g_{\mathrm{re}}(\varepsilon,t)=\frac{vf(\varepsilon,t)}{\min[\xi(\varepsilon,t),e_{\mathrm{tar}}]}\sin^2(\theta_{\mathrm{re}}/2)\,\Theta(\varepsilon-e\Phi). \tag{16b}$$

The total current of escaping electrons J and the total target charge Q are calculated then as integrals over the distribution function and time:

$$J(t)=e\int_{\Phi(t)}^{\infty}(g_{\mathrm{re}}+g_{\mathrm{fr}})\,d\varepsilon, \tag{17a}$$

$$Q(t)=\int_0^t J(t')\,dt'. \tag{17b}$$

The formation of the potential barrier at the target surface is described in the next section.

D. The potential barrier

The potential barrier model for a semi-infinite target was described in Ref. [13]. It has two origins, the electron thermal motion and the target polarization:

$$\Phi(t)=\phi_{\mathrm{th}}(t)+\phi_E(t). \tag{18}$$

The thermal potential ϕ_{th} is due to the negative charge created by hot electrons in the Debye layer above the target surface $\lambda_{\mathrm{Dh}}=(\epsilon_0 T/ne^2)^{1/2}$, where e is the electron charge and ϵ_0 is the vacuum permittivity. The electrostatic potential ϕ_E is due to the positive charge left on the target surface by escaped fast electrons. This model applies also to thin targets assuming that the potential Φ is the same at the two ejection surfaces. This is consistent with our initial hypothesis of a homogeneous hot electron cloud. Then the electrostatic potential ϕ_E is calculated by accounting for the two current contributions from the front and rear sides. The thermal potential calculation accounts for the fact that the electron cloud volume is limited by the target thickness according to Eq. (11b).

According to Ref. [13] the height of the thermal potential barrier in a thick target depends on the ratio of the Debye length to the average cloud radius R_{av}:

$$\frac{e\phi_{\mathrm{th}}}{T_h}=\frac{\lambda}{\sqrt{\lambda^2+1}}\ln\frac{\sqrt{\lambda^2+1}+1}{(\sqrt{\lambda^2+1}-\lambda)\lambda}-\ln(2\lambda), \tag{19}$$

where $\lambda=\sqrt{2\mathrm{e}}\lambda_{\mathrm{Dh}}/R_{\mathrm{av}}$ and e is the base of the natural logarithm.

Equation (19) is modified for very thin targets where e_{tar} is smaller than λ_{Dh} and a significant part of hot electrons circulates in the Debye layer outside the target. Calculations presented in Appendix A result in the following expression:

$$\begin{aligned}\frac{e\phi_{\mathrm{th}}}{T_h}=\Bigg\{&\frac{1}{c_1c_2}\Big[c_2\Big(\sqrt{c_2^2+1}-c_2\Big)+\sinh^{-1}c_2\Big]\\&-2\Bigg[\ln 2-1+\frac{b}{\sqrt{b^2+1}}\ln\Big(\sqrt{b^2+1}-b\Big)\Bigg]\\&+2\Bigg[\frac{b}{\sqrt{b^2+1}}\ln\Bigg(\frac{\sqrt{b^2+1}\sqrt{c_2^2+1}-bc_2+1}{c_1}\Bigg)\\&-\frac{\sqrt{c_2^2+1}}{c_1}-\frac{b}{c_1}-\ln c_1+\sinh^{-1}c_2\Bigg]\Bigg]\Bigg\}.\end{aligned} \tag{20}$$

Here $b=c_1-c_2$ and the constants α, c_1, and c_2 are defined as follows:

$$\alpha=2\frac{\lambda_{\mathrm{Dh}}^2}{e_{\mathrm{tar}}^2}\left(\sqrt{1+2\frac{e_{\mathrm{tar}}^2}{\lambda_{\mathrm{Dh}}^2}}-1\right), \tag{21a}$$

$$c_1=2\lambda_{\mathrm{Dh}}^2/\alpha\, e_{\mathrm{tar}}R_{\mathrm{av}}, \quad c_2=e_{\mathrm{tar}}/2R_{\mathrm{av}}. \tag{21b}$$

For the intermediate thicknesses $e_{\mathrm{tar}}\sim\lambda_{\mathrm{Dh}}$ we use the interpolation formula by taking a minimum of Eqs. (19) and (20). Figure 4 shows the interpolated potential for the ratio $R_{\mathrm{av}}/\lambda_{\mathrm{Dh}}=100$.

The electrostatic potential is defined according to Ref. [13]. The ejected electron leaves a positive charge at the target surface, which spreads at a speed of light across the whole target surface if the target is made of a conducting material.

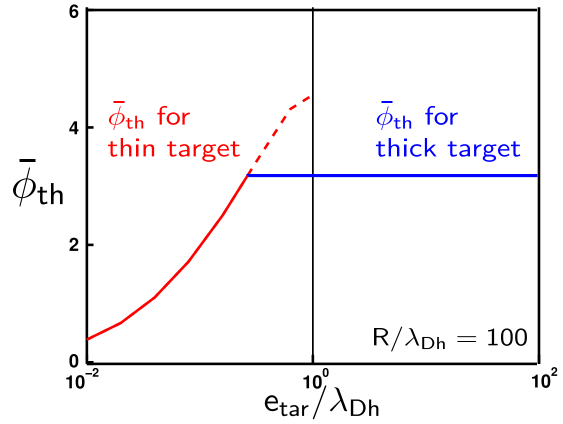

FIG. 4. Dependence of the thermal potential ϕ_{th}/T_h on the target thickness for the ratio $R_{av}/\lambda_{Dh} = 100$. The left red line is the potential for a thin target (20) valid if $e_{tar}/\lambda_{Dh} < 1$. The right blue line is the potential for a thick target given by Eq. (19).

For insulating target, this charge repartition is limited to the hot electron cloud radius. A finite size of the target limits this charge redistribution leading to an increase of the electrostatic potential and suppression of the ejection current. We assume that the potential is same on both sides of the target, which is a reasonable hypothesis if the target thickness is smaller than its transverse dimension:

$$\phi_E(t) = \frac{1}{2\pi\epsilon_0}\int_0^t \frac{J(t')}{\min\left[R_{av}(t') + c(t-t'), r_{tar}\right]}\,dt'. \tag{22}$$

The model described in this section is realized numerically as a Fortran90 program CHOCOLAT2.F90 as described in Appendix B.

III. COMPARISONS AND RESULTS

A. Comparison with previous model

Before discussing our experimental results, we demonstrate that our model is compatible with the previous results [12,13]. Figure 5 presents the target charge as a function of the pulse duration calculated with the previous model CHOCOLAT.F90, our model CHOCOLAT2.F90, and experimental data for thick copper, aluminum, and tantalum targets. The results are rather similar with the model showing a smoother transition between the limit of very short pulses (explosive regime). A weak dependence on the laser pulse duration and on the target material observed in experiments is improved in our model. We notice a global error of a factor of two.

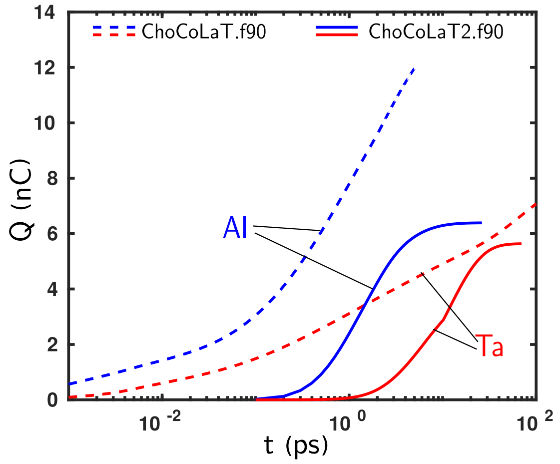

FIG. 6. Time evolution of the target charging obtained with the previous model CHOCOLAT.F90 and with our model CHOCOLAT2.F90. Target parameters: aluminum, $r_{tar} = 5$ mm, $e_{tar} = 3$ mm. Laser parameters: $t_{las} = 30$ fs, $\mathcal{E}_{las} = 80$ mJ, $r_{las} = 6\,\mu$m, $\eta = 40\%$, and $\lambda_{las} = 0.8\,\mu$m.

The differences between models become more apparent when considering the temporal evolution of the target charge as the electron cooling is described more accurately; see Fig. 6. In the previous model the ejection current stops at the time $t_{las} + t_{ee}(T_0)$. In our model, the current ejection is delayed and the saturation time is defined by the cooling time of escaping electrons, which are hotter than the average. The ejection time can still be estimated by $t_{las} + t_{ee}(T_0)$: the magnitude order is still correct.

As our model operates with distribution function instead of averaged values, it provides access to such characteristics as electron energy distribution function inside and outside the

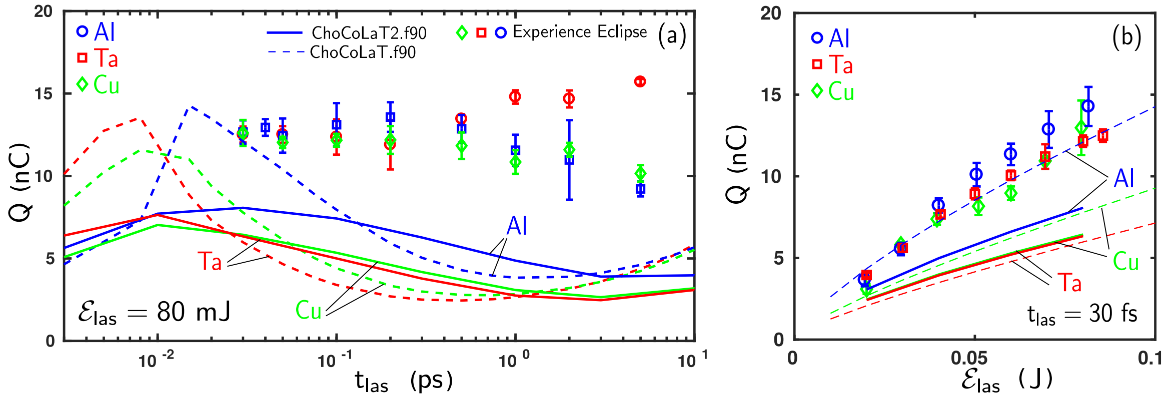

FIG. 5. Comparison of the measured target charge (symbols) and the model predictions (dashed curves for the previous model CHOCOLAT.F90 and solid curves for our model CHOCOLAT2.F90) for scans on the laser pulse duration (a) and on the laser energy (b): t_{las} varies from 30 fs to 5 ps, $\mathcal{E}_{las}$ varies from 20 to 80 mJ, $r_{las} = 6\,\mu$m, laser absorption $\eta = 40\%$, and $\lambda_{las} = 0.8\,\mu$m. Targets are made of aluminum (blue), copper (green), and tantalum (red).

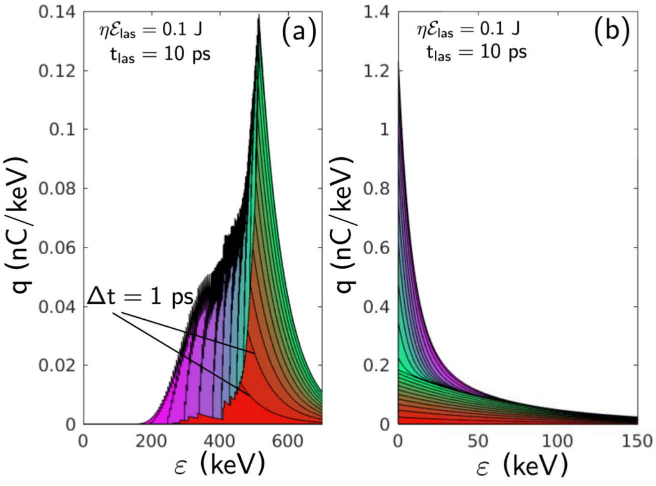

FIG. 7. Time evolution of distribution as a function of ejected electron before (a) and after (b) the potential barrier in the sustained regime. Target parameters: aluminum, $r_{\rm tar} = \infty$, $e_{\rm tar} = 0.1$ mm. Laser parameters: $t_{\rm las} = 10$ ps, $\eta\mathcal{E}_{\rm las} = 100$ mJ, $r_{\rm las} = 6\,\mu$m, and $\lambda_{\rm las} = 0.8\,\mu$m.

target. The energy distributions of ejected electrons depend on the laser pulse duration and intensity. Figure 7 shows the time evolution of ejected electrons before and after the potential barrier for the regime of sufficiently long laser pulses:

$$q_{\rm in}(\varepsilon, t) = e\int_0^t [g_{\rm fr}(\varepsilon, t') + g_{\rm re}(\varepsilon, t')]\, dt', \tag{23a}$$

$$q_{\rm out}(\varepsilon, t) = e\int_0^t [g_{\rm fr}(\varepsilon + e\Phi, t') + g_{\rm re}(\varepsilon + e\Phi, t')]\, dt'. \tag{23b}$$

The time evolution is represented by color variation from red to green and purple. In this sustained regime, the potential barrier stays constant and the tail of distribution function is refilled by the laser. The electrons are losing a large amount of energy while crossing the potential barrier. The residual energy of ejected electrons is comparable with their temperature inside the target. This is not the case of short laser pulses corresponding to the explosive regime, represented in Fig. 8. In this case, the tail of distribution function is completely depleted. Then, due to the electron cooling, the potential barrier drops and new hot electrons are able to escape.

This delayed emission in the explosive regime produces escaped electrons with a very small residual energy compared to the temperature inside the target. The residual energy of ejected electrons is inversely proportional to the ejection current amplitude and proportional to the potential drop speed. At the limit, electrons with an instantaneous ejection time during the potential drop would have no energy remaining.

B. Comparison of the model with thin target experiments

Here we compare the model predictions with experiments conducted with thin aluminum targets. According to Fig. 1, a stopping range of a 600 keV electron is 1 mm. So the target thickness was varied from 20 μm to 3 mm in order to cover both the thick and thin regimes. The laser parameters are the

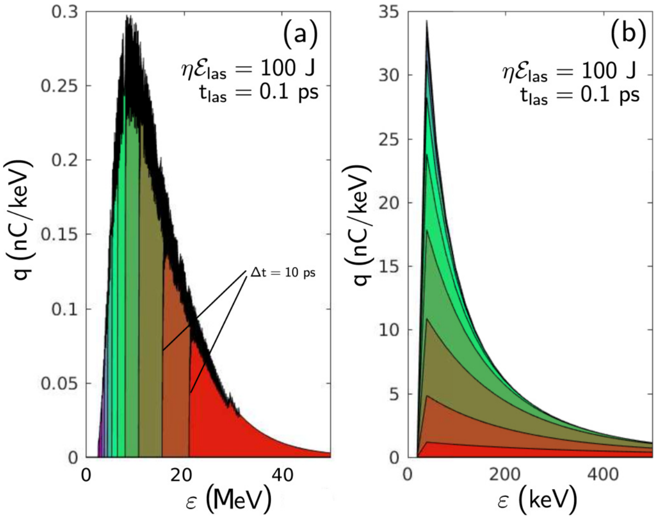

FIG. 8. Time evolution of distribution as a function of ejected electron before (a) and after (b) the potential barrier in the explosive regime. Target parameters: aluminum, $r_{\rm tar} = 10$ mm, $e_{\rm tar} = 0.1$ mm. Laser parameters: $t_{\rm las} = 0.1$ ps, $\eta\mathcal{E}_{\rm las} = 100$ J, $r_{\rm las} = 6\,\mu$m, and $\lambda_{\rm las} = 0.8\,\mu$m.

same as described in Refs. [11,12] and shown in Fig. 5. The experimental results are presented in Fig. 9.

We observe overall good agreement of the model and the experiment: (i) the accumulated charge increases as the target thickness decreases, (ii) the charge decreases as the pulse duration increases, and (iii) the charge increases with the laser pulse energy. There is a quantitative agreement in what concerns the dependence on the laser pulse energy and target thickness. The dependence on the pulse duration is less satisfactory: the target charge is independent on the pulse duration of less than 1 ps, while the model shows a gradual decrease of the charge for shorter pulse durations. This difference can be explained by the simplified form of our kinetic equation (1), which maintains the electron energy but decreases their number during the cooling time. For the parameters of this experiment, the hot electron energy does not exceed 100 keV, and the average penetration range is $\sim 50\,\mu$m. So the effect of the rear surface appears at the bottom of our scan range.

C. Analysis of the model predictions

It is tempting to assume that the charge accumulation on the target is doubled because of the second ejection surface at rear side. This is not, however, a complete answer. Figure 10, top line, shows a fraction of the charge ejected from the rear surface, $Q_{\rm re}/Q$, as a function of the target thickness $e_{\rm tar}$ and the laser parameters $t_{\rm las}$ and $\eta\mathcal{E}_{\rm las}$. It the intensity is high enough, the hot electrons reach the rear side, and we observe a current repartition between front and rear surface. Figure 10, bottom line, presents a ratio of the accumulated charge for a thin and a semi-infinite target. For a high laser intensity, this ratio attains a factor of five. The contribution to this charge increase has two origins. The first one is an increase of the electron ejection cone from the thick target value to a maximum of 4π sr. This increase includes the rear surface contribution and can increase the target charge accumulation from a factor of three for aluminum

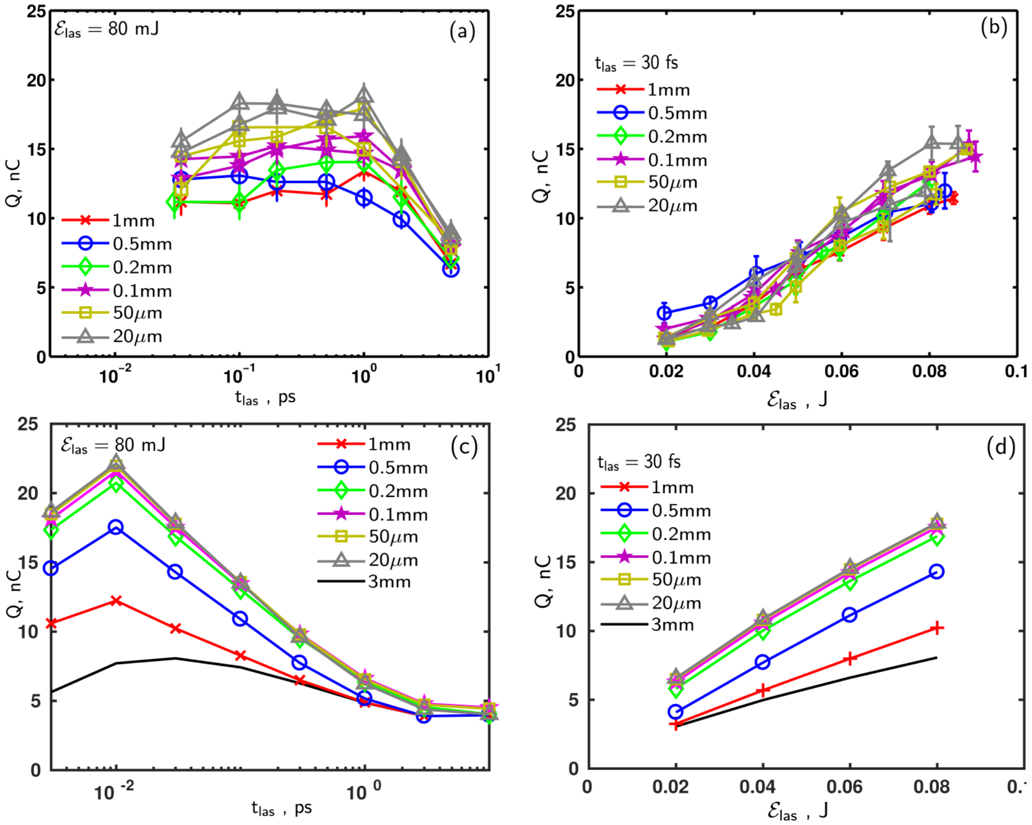

FIG. 9. (a, b) Experimental measurements of the target charge Q on laser parameters. Aluminum target with a thickness varying from 20 μm to 1 mm (color code). (c, d) Model calculations for the same parameters. (a–c) Dependence on the laser pulse duration $t_{\rm las}$ at laser energy $\mathcal{E}_{\rm las} = 80$ mJ, $r_{\rm las} = 6\,\mu$m, and $\eta = 40\%$. (b–d) Dependence on the laser pulse energy $\mathcal{E}_{\rm las}$ for $t_{\rm las} = 30$ ps, $r_{\rm las} = 6\,\mu$m, and $\eta = 40\%$.

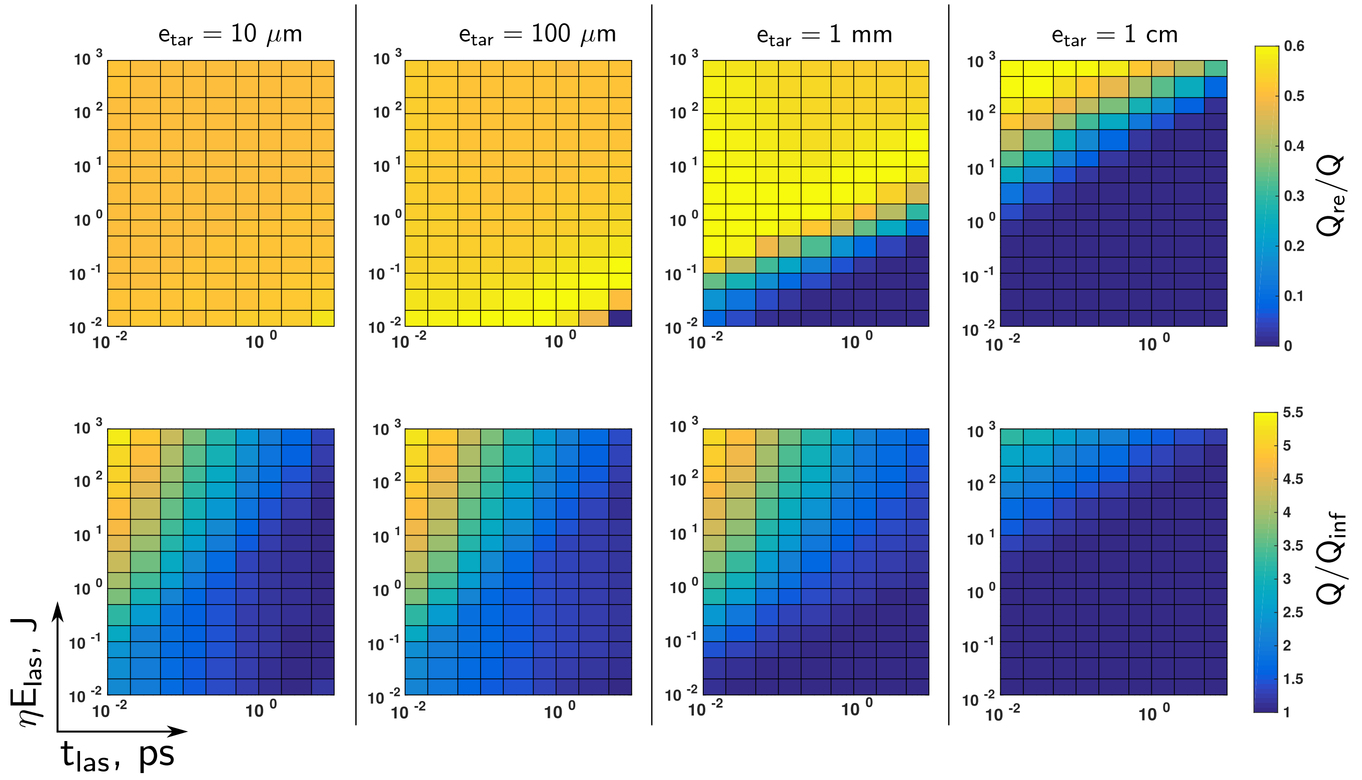

FIG. 10. Top line: fraction of the total charge ejected from the rear surface, $Q_{\rm re}/Q$ in function on $t_{\rm las}$ and $\eta\mathcal{E}_{\rm las}$. Bottom line: the same for the ratio $Q/Q_{\rm inf}$. Target parameters: aluminum, $r_{\rm tar} = \infty$, target thickness is shown. Laser parameters: $r_{\rm las} = 6\,\mu$m and $\lambda_{\rm las} = 0.8\,\mu$m.

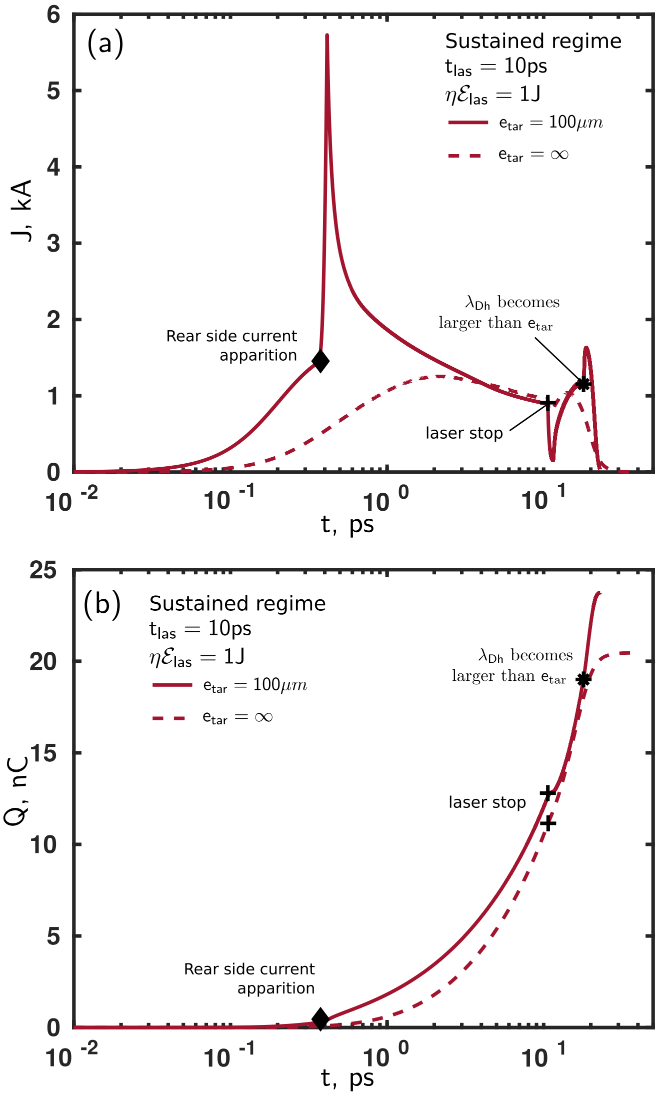

FIG. 11. Time evolution of the ejected current (a) and the charge (b) in sustained regime. Target parameters: aluminum, $r_{tar} = \infty$, $e_{tar} = 0.1$ mm (solid line), $e_{tar} = \infty$ (dashed line). Laser parameters: $t_{las} = 10$ ps, $\eta\mathcal{E}_{las} = 0.1$ J, $r_{las} = 6\,\mu$m, and $\lambda_{las} = 0.8\,\mu$m.

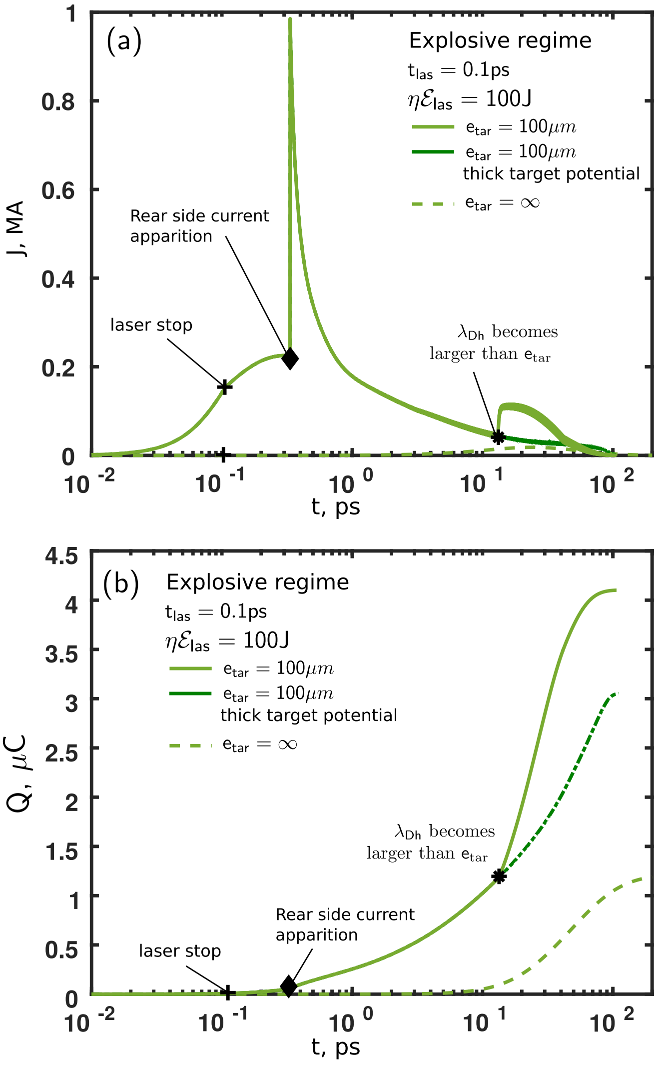

FIG. 12. Time evolution of the ejected current (a) and the charge (b) in the explosive regime. Target parameters: aluminum, $r_{tar} = \infty$, $e_{tar} = 0.1$ mm (full line), $e_{tar} = \infty$ (dashed line). Laser parameters: $t_{las} = 0.1$ ps, $\eta\mathcal{E}_{las} = 100$ J, $r_{las} = 6\,\mu$m, and $\lambda_{las} = 0.8\,\mu$m.

to two for heavy materials. The second contribution appears for very thin targets only when their thickness is smaller than the hot electron Debye length. This corresponds to a drop of the potential barrier and a current increase.

Those two contributions act differently considering the sustained or explosive regime. For the sustained regime, the charge accumulation and the ejection current are shown in Fig. 11. Two cases are plotted: one for a semi-infinite target, a second for a target of 100 μm thickness. The initial current from a thin target is stronger than from thick one because the front ejection angle is larger. A peak of current corresponds to the electron ejection from the rear side. In this regime, the ejection current is controlled by the electrostatic potential, which maintains the feedback control. During the cooling time, the Debye length increases and exceeds the target thickness. This produce a potential barrier drop and a second current peak. However, its impact is limited since it concerns only a small part of the charge. For this reason, in a sustained regime, there is no much difference between thin or thick targets.

Similar analysis for the explosive regime is shown in Fig. 12. Here the sequence of events comes in a different order. The laser pulse ends before the rear side current appears and the potential swaps from thick to thin regime. The geometric contribution from the emission angle to the current increases the accumulated charge by a factor of three. The ejection angle cone increases from 70° to 180°. This increase is not affected by the electrostatic potential. The thermal potential drops at 10 p and leads to increase the charge from 3000 nC (for a semi-infinite target) to 4000 nC. This increase could be even higher for thinner targets or more intense laser pulses: the thin potential formula would apply sooner in the hot electron cloud dynamics.

IV. CONCLUSION

The kinetic model is able to predict the target charging as a function of the laser pulse parameters for thick and thin targets. The characteristic control parameter is the ratio of the hot electron mean-free path to the Debye length. This model is validated by the comparison with a series of dedicated experiments. The energy distribution of ejected electrons is calculated, it might be useful for analysis of the electromagnetic emission from the target in the THz domain. An example of temporal evolution of the electron distribution function inside the target can be found in the Supplemental Material [23]. A numerical code presented in Appendix B could be used for quick and sufficiently accurate evaluation of the target for given experimental conditions.

ACKNOWLEDGMENTS

This work has been carried out within the framework of the EUROfusion Consortium and has received funding from the Euratom research and training program 2014–2018 under Grant Agreement No. 633053. The views and opinions expressed herein do not necessarily reflect those of the European Commission. This study has been carried out with financial support from the French state, managed by the French National Research Agency (ANR) in the frame of "the Investments for the future" Programme IdEx Bordeaux–LAPHIA (ANR-10-IDEX-03-02).

APPENDIX A: THIN TARGET THERMAL POTENTIAL CALCULATION

Calculation of the potential of a thin target is similar to the case of a thick target presented in Appendix B [13]. The hot electron density outside the target is calculated by solving a one-dimensional Poisson equation [24–27]. Then this electron density is limited radially to a cylinder of a radius R_h and used for calculation of a three-dimensional potential distribution. For thin targets, the ratio of the Debye length to the target thickness defines the charge repartition.

1. Thin target density profile

Let us consider the case of a very thin target, $e_{\text{tar}} \ll \lambda_{\text{Dh}}$, where the electron density is constant inside the target. We solve the Poisson equation with electrons following a truncated Boltzmann distribution on both sides of the target. This is graphically illustrated in Fig. 13 where Fig. 13(a) shows the electron distribution for a semi-infinite target; Fig. 13(b) presents superposition of these profiles on both sides which are connected to a constant density inside the target. The unknown electron density inside is estimated from the charge conservation. Figure 13(c) presents the potential distribution. It has a symmetric parabolic form inside the target.

The Poisson-Boltzmann equation reads

$$\epsilon_0 \partial_\xi^2 \phi_{\text{th}} = -e[n_i - n_e \exp(e\phi_{\text{th}}/T)], \tag{A1}$$

where ϵ_0 is the vacuum dielectric permittivity. The ion density is described by a Heaviside function, $n_i = (N/V)\Theta(\xi \pm e_{\text{tar}}/2)$, where $\xi = 0$ defines the target center. Equation (A1) is simplified by applying the following normalization: $\hat{\phi} = e\phi_{\text{th}}/T$, $\hat{e}_{\text{tar}} = e_{\text{tar}}/\lambda_{\text{Dh}}$, and $\hat{\xi} = \xi/\lambda_{\text{Dh}}$. The derivatives on $\hat{\xi}$ are noted with a prime. One obtains

$$\hat{\phi}'' = \exp\hat{\phi} \quad \text{if } |\hat{\xi}| > \hat{e}_{\text{tar}}/2, \tag{A2a}$$

$$\hat{\phi} = \hat{\phi}_0 - \alpha\hat{\xi}^2 \quad \text{if } |\hat{\xi}| < \hat{e}_{\text{tar}}/2. \tag{A2b}$$

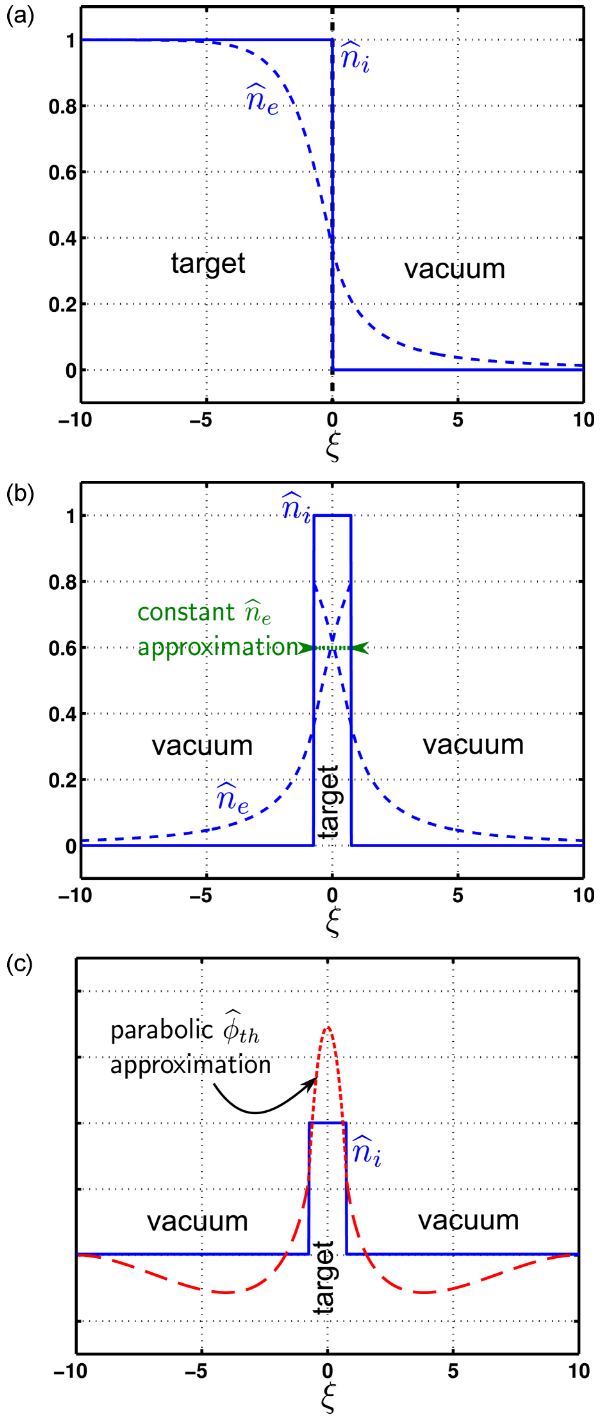

FIG. 13. (a) Density along laser axes in case of semi-infinite target. (b) Electron density along the laser axes for a combination of two semi-infinite targets with the constant density approximation. (c) Parabolic potential from the constant electron density inside the target.

The inside solution is obtained by taking the second derivative of the parabolic potential:

$$\hat{n}_e = 1 - 2\alpha \text{ if } |\hat{\xi}| < \hat{e}_{\text{tar}}, \tag{A3}$$

where $\hat{\phi}_0$ is the normalized potential at the middle of the target and α is a integration constant to be found.

The outside solution is obtained by integrating twice Eq. (A2a). We obtain

$$\hat{\phi} = -2\ln(\hat{\xi}/\sqrt{2} + k) \quad \text{if } |\hat{\xi}| > \hat{e}_{\text{tar}}/2, \tag{A4a}$$

$$\hat{n}_e = (\hat{\xi}/\sqrt{2} + k)^{-2} \quad \text{if } |\hat{\xi}| > \hat{e}_{\text{tar}}/2, \tag{A4b}$$

where k is the second integration constant to be determined, while the first one was found with the boundary conditions at infinity $\hat{\phi}(\pm\infty) = -\infty$ and $\hat{\phi}'(\pm\infty) = 0$.

The continuity equations for, respectively, the density, the potential, and its derivative are at $\hat{\xi} = \hat{e}_{\text{tar}}/2$:

$$1 - 2\alpha = [\hat{e}_{\text{tar}}/(2\sqrt{2}) + k]^{-2}, \tag{A5a}$$

$$\hat{\phi}_0 - \alpha\frac{\hat{e}_{\text{tar}}^2}{4} = -2\ln[\hat{e}_{\text{tar}}/(2\sqrt{2}) + k], \tag{A5b}$$

$$(\alpha\hat{e}_{\text{tar}})^2 = 2\exp\left(\hat{\phi}_0 - \alpha\frac{\hat{e}_{\text{tar}}^2}{4}\right). \tag{A5c}$$

Note that the continuity equation (A5c) on $\hat{\phi}'$ corresponds to the electroneutrality. The system is solved to find k and α, which are required for the density profile:

$$\alpha = \frac{2}{\hat{e}_{\text{tar}}^2}\left(\sqrt{1 + \frac{\hat{e}_{\text{tar}}^2}{2}} - 1\right), \tag{A6a}$$

$$k = \frac{\sqrt{2}}{\alpha\hat{e}_{\text{tar}}} - \frac{\hat{e}_{\text{tar}}}{2\sqrt{2}}. \tag{A6b}$$

We summarize the density equations:

$$\hat{n}_e = \left[(\hat{\xi} - \hat{e}_{\text{tar}}/2)\frac{1}{\sqrt{2}} + \frac{\sqrt{2}}{\alpha\hat{e}_{\text{tar}}}\right]^{-2} \quad \text{if } \hat{\xi} > \hat{e}_{\text{tar}}/2, \tag{A7a}$$

$$\hat{n}_e = 1 - 2\alpha \quad \text{if } \hat{\xi} < \hat{e}_{\text{tar}}/2. \tag{A7b}$$

2. Thin target potential profile

The zone of interest of the potential is the center of the target. As it is thinner than the hot Debye length, we can assume that the middle value of ϕ_{th} is the barrier value encountered by all hot electrons. So we limit our calculation to this position only. We assume the density to be constant in the target plane over the hot electrons cloud radius R, so we can use the potential formula from homogeneously charged disk [28], integrated over the axis ξ to sum all the contributions:

$$\phi_{\text{th}} = \int_{-\infty}^{+\infty}\frac{e[n_i(\xi) - n_e(\xi)]}{2\epsilon_0}(\sqrt{R^2 + \xi^2} - |\xi|)d\xi. \tag{A8}$$

Here the same normalization applies as in Eq. (A1). We introduce the variable $\zeta = \hat{\xi}/\hat{R}$ and the notation $\bar{e}_{\text{tar}} = \hat{e}_{\text{tar}}/\hat{R} = e_{\text{tar}}/R$:

$$\hat{\phi}_{\text{th}} = \int_{-\infty}^{+\infty}\frac{[\hat{n}_i(\zeta) - \hat{n}_e(\zeta)]}{2}(\sqrt{1 + \zeta^2} - |\zeta|)d\zeta. \tag{A9}$$

The integral is split in half because of the steplike ion density and the problem symmetry at $\zeta = 0$. Then the contributions with ξ positive and negative are equal:

$$\begin{aligned}\hat{\phi}_{\text{th}} = {} & 2\int_0^{\bar{e}_{\text{tar}}/2}\alpha\hat{R}^2(\sqrt{1 + \zeta^2} - \zeta)d\zeta \\ & - 2\int_{\bar{e}_{\text{tar}}/2}^{+\infty}\frac{\sqrt{1 + \zeta^2} - \zeta}{\left[(\zeta - \bar{e}_{\text{tar}}/2) + \frac{2}{\alpha\hat{e}_{\text{tar}}\hat{R}}\right]^2}d\zeta.\end{aligned} \tag{A10}$$

Those integrals have solutions, with $b = \frac{2}{\alpha\hat{e}_{\text{tar}}\hat{R}} - \frac{\bar{e}_{\text{tar}}}{2}$:

$$\begin{aligned}\hat{\phi}_{\text{th}} = {} & \alpha\hat{R}^2[\zeta(\sqrt{\zeta^2 + 1} - \zeta) + \sinh^{-1}(\zeta)]_0^{\bar{e}_{\text{tar}}/2} \\ & - 2\left[\frac{b}{\sqrt{b^2 + 1}}\ln\left(\frac{\sqrt{b^2 + 1}\sqrt{\zeta^2 + 1} - b\zeta + 1}{b + \zeta}\right)\right. \\ & \left. - \frac{(\sqrt{\zeta^2 + 1} + b)}{b + \zeta} - \ln(b + \zeta) + \sinh^{-1}(\zeta)\right]_{\bar{e}_{\text{tar}}/2}^{+\infty}.\end{aligned} \tag{A11}$$

Using the relation $\sinh^{-1}(\infty) - \ln(\infty) = \ln(2)$, we recover Eq. (20).

APPENDIX B: ChoCoLaT2.f90

1. Code description

ChoCoLaT2.f90 has a similar architecture than its previous version [13]. After an initialization step, where the files are read and created, the static values are calculated such as t_{life}, T, or f_{las}, and the code enters into a *while* loop. This loop iterates calculations of the distribution function, then averages it, and calculates the potential and then the ejection currents. The outputs are generated during this loop at a chosen frequency. The code is stopped when N is smaller than $0.001 \times Q$ (while the laser is off): when the hot electron cloud is empty enough to not affect the charge whatever the possible evolutions.

2. User commands

Compilation command: gfortran -O3 ChoCoLaT2.f90

Launch command:./a.out 1234 {arguments} The number 1234 is the four-digit number of the input file and the arguments have the format: *.****E±**. For this code source, there are tree optional arguments: e_{tar}, t_{las}, and E_{las}.

The code takes the input in this priority order:

(1) Arguments of the launch command line. Manageable in the code, l. 205-214.

(2) Input file: its name is input_1234.txt.

(3) Default file: its name is input_0000.txt.

(4) Default values. Manageable in the code, l. 176-195.

3. Outputs

The code has two kinds of output. The short one is the file named *output_scalar*_1234*.txt*. It contains energetic averages of R_{av} (μm), λ_D (μm), T (keV), N (nC), ϕ_{th} (keV), ϕ_E (keV), J_{fr} (kA), J_{re} (kA), and Q (nC) versus time. The frequency of the output is set by the parameter $diag\ s$ in the input file. The time step of the diagnostic is then $dt \times diag\ s$.

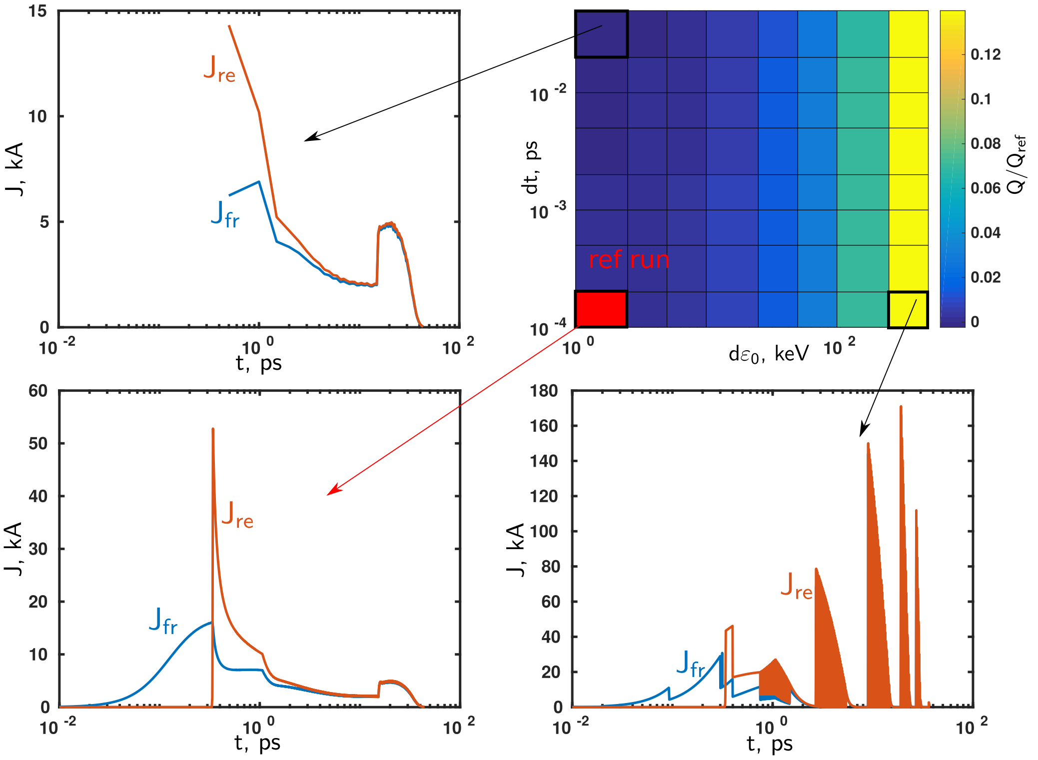

FIG. 14. The charge obtained over the reference one with the best resolution ($dt = 10^{-4}$ ps and $d\varepsilon_0 = 6.5$ keV) for various time and energy resolution. Current evolution of the reference case and two unresolved cases (low time resolution or low energy resolution). Target parameters: aluminum, $r_{\mathrm{tar}} = 10$ mm, $e_{\mathrm{tar}} = 0.1$ mm. Laser parameters: $t_{\mathrm{las}} = 1$ ps, $\mathcal{E}_{\mathrm{las}} = 10$ J, $r_{\mathrm{las}} = 6\,\mu$m, $\eta = 40\%$, and $\lambda_{\mathrm{las}} = 0.8\,\mu$m.

The heavy diagnostic is tree distribution functions of electrons inside the target, escaped by the front side and escaped by the rear side (before the potential barrier). The files are named, respectively, output_f_in___1234.txt, output_f_Jre__1234.txt, and output_f_Jre__1234.txt. The time step of this diagnostic is then $dt \times diag\ h$, manageable in the input file.

If $diag\ s$ and/or $diag\ h$ are (is) set to zero, the associated diagnostics are cut to save running time and space disk.

4. Convergence

The temporal scheme is a basic Euler scheme. The CFL must be accounted for with the try-error method to get a satisfying result. Figure 14 provides an example of the convergence map with the usual troubleshooting due to a bad resolution. Note that the error will not appear in the charge value, that does not vary much, but in the current evolution. There are tree variables that control the resolution in the input file: dt is set directly. $d\varepsilon$ is changing with the simulation parameter, since it involves T_0:

$$d\varepsilon = T_h \times Nb_{T_0}/N_\varepsilon. \tag{B1}$$

Nb_{T_0} and N_ε are tunable in the input file. The first sets the maximal value of ε as a number of T_0. As our model focuses on the tail of the distribution function, the typical value of Nb_{T_0} is 10. The second is the number of points of the distribution function. As our model needs a proper description of the low- and medium-energy electrons for the potential calculation, set a typical value of 1000. This number increases with the laser intensity.

---

[1] J. S. Pearlman *et al.*, Appl. Phys. Lett. **31**, 414 (1977).
[2] M. J. Mead *et al.*, Rev. Sci. Instrum. **75**, 4225 (2004).
[3] C. G. Brown Jr. *et al.*, J. Phys.: Conf. Ser. **112**, 032025 (2008).
[4] Z. Y. Chen *et al.*, Phys. Plasmas **19**, 113116 (2012).
[5] C. G. Brown Jr., T. J. Clancy, D. C. Eder, W. Ferguson, and A. L. Throop, EPJ Web Conf. **59**, 08012 (2013).
[6] D. C. Eder *et al.*, Lawrence Livermore National Laboratory Report, LLNL-TR-411183 (2009).
[7] C. Courtois *et al.*, Phys. Plasmas **16**, 013105 (2009).
[8] S. Fujioka *et al.*, Sci. Rep. **3**, 1170 (2013).
[9] J. J. Santos *et al.*, New J. Phys. **17**, 083051 (2015).
[10] V. Tikhonchuk *et al.*, Phys. Rev. E **96**, 023202 (2017).
[11] J.-L. Dubois *et al.*, Phys. Rev. E **89**, 013102 (2014).
[12] A. Poyé *et al.*, Phys. Rev. E **91**, 043106 (2015).
[13] A. Poyé *et al.*, Phys. Rev. E **92**, 043107 (2015).
[14] J. C. Kieffer *et al.*, Appl. Phys. B **74**, S75 (2002).
[15] G. Korn *et al.*, Opt. Lett. **27**, 866 (2002).
[16] S. Fourmaux, C. Serbanescu, R. E. Kincaid Jr., A. Krol, and J. C. Kieffer, Appl. Phys. B **94**, 569 (2008).
[17] R. Fabbro *et al.*, Phys. Fluids **28**, 1463 (1985).
[18] F. N. Beg *et al.*, Phys. Plasmas **4**, 447 (1997).
[19] S. C. Wilks, W. L. Kruer, M. Tabak, and A. B. Langdon, Phys. Rev. Lett. **69**, 1383 (1992).

[20] P. Gibbon, *Short Pulse Laser Interaction with Matter, an Introduction* (World Scientific, London, 2005).

[21] K. Kanaya and S. Okayama, J. Phys. D: Appl. Phys. **5**, 43 (1972).

[22] http://physics.nist.gov/PhysRefData/Star/Text/ESTAR.html.

[23] See Supplemental Material at http://link.aps.org/supplemental/10.1103/PhysRevE.98.033201 for a movie of the distribution function and its source code and input file.

[24] P. Mora, Phys. Rev. Lett. **90**, 185002 (2003).

[25] J. E. Bateman *et al.*, RAL Technical Reports, RAL-TR-2012-005 (2012).

[26] J. E. Crow, J. Plasma Phys. **14**, 65 (1975).

[27] J. Schreiber, F. Bell, F. Gruner, U. Schramm, M. Geissler, M. Schnurer, S. Ter-Avetisyan, B. M. Hegelich, J. Cobble, E. Brambrink, J. Fuchs, P. Audebert, and D. Habs, Phys. Rev. Lett. **97**, 045005 (2006).

[28] J. D. Jackson, *Classical Electrodynamics* (Wiley, New York, 1975).